Western Gondwana imaged by S receiver-functions (SRF): new results on Moho, MLD (mid-lithospheric discontinuity) and LAB (lithosphere-asthenosphere boundary)

Lin Liu[1,2,3], Simon L. Klemperer[2], Alexander R. Blanchette[2]

[1]Frontiers Science Center for Deep Ocean Multispheres and Earth System, Key Lab of Submarine Geosciences and Prospecting Techniques, MOE and College of Marine Geosciences, Ocean University of China, Qingdao 266100, China.

[2]Department of Geophysics, Stanford University, Stanford, CA 94305, USA.

[3]Laboratory for Marine Mineral Resources, Qingdao National Laboratory for Marine Science and Technology, Qingdao 266237, China

Abstract

We study the Moho, the mid-lithospheric discontinuity (MLD), and the lithosphere-asthenosphere boundary (LAB) from southern Africa to northern Arabia, from Archean cratons to active rifts, at 1° resolution using our comprehensive new database of shear-wave receiver functions (SRFs). The good agreement between the Moho depth obtained from our SRFs and published P-wave receiver function (PRF) results provides confidence that our images of deeper lithospheric discontinuities are robust, including boundaries not normally visible on PRFs. We map the Moho and a deeper negative velocity gradient (NVG) almost everywhere we have data coverage. Our synthetic tests and comparisons of SRFs processed with and without deconvolution, and with varying filter parameters, indicate the observed NVG represents earth structure, not a processing artifact. Depth comparisons with seismic tomography and tectonothermal age studies suggest the NVG represents the MLD beneath Archean cratons but

represents the LAB beneath non-cratonic regions. Both preserved crustal thickness and lithospheric thickness in the Nubia-Somalia-Arabia plates are statistically thinner for Phanerozoic and late Proterozoic terranes and older regions reactivated during these eras, than for cratons not reworked since the early Proterozoic or Archean. In contrast, NVG depth is uniform for all tectonothermal ages, though with a possible increase in amplitude with age. The equivalence of NVG depth and LAB depth in Phanerozoic lithosphere suggests that low-wavespeed compositions are frozen into the lithosphere as it thickens by cooling, forming our observed MLD at the present day.

1. Introduction

The lithosphere, Earth's rigid outermost shell overlying a lower–viscosity asthenosphere, ranges in thickness from a few kilometers at ocean spreading centers to 250–300 km in continental cratons (e.g. Artemieva, 2009; 2011). The two fundamental seismic discontinuities in the crust and uppermost mantle are the Mohorovicic discontinuity (Moho) that marks a compositional change from fractionated felsic-to-mafic rocks to ultramafic peridotites, and the lithosphere-asthenosphere boundary (LAB) that marks a rheological change as measured over geological time from strong (plate-like) to weak (convective asthenosphere).

This rheological change occurs around the conductive-adiabatic geotherm intersection, the thermal layer in the mantle spanning tens of kilometers across which the mode of heat transfer gradually changes from conduction to convection (e.g. Artemieva, 2011; Rychert et al., 2020). Typical thickness of continental lithosphere inferred from Earth's thermal structure (Artemieva, 2006) increases with tectonothermal age from 60–80 km in active extensional regions to 100–160 km in Meso- and Neoproterozoic and Paleozoic terranes to 200–300 km in Archean and Paleoproterozoic cratons (Artemieva, 2011). Exceptions include Archean cratons affected by Phanerozoic tectono-magmatic events (e.g. Wyoming and Sino-Korean cratons) where lithospheric thickness does not exceed 120–150 km. The seismic lithosphere is a seismic high-wavespeed layer, or 'lid', above a low-wavespeed zone (or 'low-velocity zone') or a gradational decrease in seismic wavespeed with depth. This boundary has been called the '8°-discontinuity' (Thybo and Perchuc, 1997) or more recently the mid-lithosphere discontinuity (MLD) (e.g. Abt et al., 2010; Aulbach et al., 2017) because it is observed in cratons at depths much less than the predicted thermal base of the lithosphere. This wavespeed structure means that different seismic methodologies will observe different apparent LAB and/or MLD depths. Long-period surface-wave seismic-tomography models for the continental lithosphere (e.g. Pasyanos, 2010) may be sensitive to the base of the thermal boundary layer, whereas intermediate-period S-to-P receiver functions (SRF) and high-frequency long-offset controlled-source data (Thybo, 2006) that best map sharp wavespeed discontinuities (e.g. Fischer et al., 2010) may be most sensitive to the top of the low-wavespeed zone that may correspond to the top of the thermal boundary layer (Artemieva, 2011). When discussing our seismic observations, we will use the term NVG (negative-velocity gradient) to avoid interpretational bias; abbreviations MLD and LAB are reserved for possible interpretations of the NVG.

1.1 Previous speculations on nature of MLD and LAB

The cratonic LAB is sometimes considered a broad thermal boundary zone, while others propose a sharper transition controlled by chemical composition, melt content or vertical variation in anisotropy (Fischer et al., 2010). Based on experimental investigations on the relationship between temperature and shear-wave speed, a wavespeed contrast sufficient to produce an observable S-to-P (Sp) conversion requires a thermal gradient of at least 20 °C/km (Faul and Jackson, 2005). Although the thermal gradient at the depth of the LAB beneath oceanic and non-cratonic areas is commonly >20 °C/km (Gholamrezaie et al., 2018), the cold cratons are generally characterized by thermal gradients <10 °C/km (Artemieva, 2006). In addition, multiple scales of mantle convection system might contribute to more-localized high thermal gradients at the LAB (King and Ritsema, 2000; Korenaga and Jordan, 2002; Fischer et al., 2010; Rychert et al., 2020).

The MLD has recently been regarded as the top layer of an intra-lithospheric low-wavespeed layer (Hansen et al., 2009b; Liu and Gao, 2018), likely a compositionally distinct layer rich in phlogopite/amphibole or a transition in elastically accommodated grain-boundary sliding, though the contribution of seismic anisotropy cannot be ruled out (Selway et al., 2015; Karato and Park, 2018). The hypothesis of partial melting contributing to the MLD in the ancient continents has been largely discarded due to the relatively low temperature, ~1000 °C, expected at the MLD (Karato and Park, 2018).

1.2 African lithosphere

Africa has experienced ~3.8 Ga of complex geodynamic history and thus allows us to investigate lithospheric structure from the Archean to the present. Africa is composed of four Archean cratons: Congo, West Africa, Kalahari, and Tanzania, flanked by younger mobile belts (Figure 1; Artemieva, 2006; Begg et al., 2009). During the Neoproterozoic, extensive assembly and reworking of lithosphere formed the Sahara Metacraton (Abdelsalam et al., 2002) and the Arabian Shield and Platform (Stern and Johnson, 2010). These terranes amalgamated with South America in the Ordovician to form western Gondwanaland from which the African plate broke away in Jurassic time (Begg et al., 2009). In the Cenozoic, African lithosphere and asthenosphere were marked by widespread volcanism, uplift, and continental rifting (Globig et al., 2016), with Red Sea rifting separating Arabia from Africa since ~30 Ma (Camp and Roobol, 1992).

We identify cratonic and non-cratonic terranes based on the global thermal model 'TC-1' of Artemieva (2006) (Figure 1c) as a better constraint on lithospheric age than surface geology; and we also separately use the tectonothermal regionalization of Griffin et al. (2013) (Figure 1d). These two terrane classifications are based on different datasets and are sub-divided into different age groupings, so do not have a one-to-one correspondence but rather represent two different opportunities to test lithospheric seismic observables against lithospheric age and origin. The wide range of tectonic ages from the oldest cratons to the youngest rift systems make Africa the ideal continent on which to address some controversial issues, such as whether a low-wavespeed intra-lithospheric layer is widespread in ancient cratons giving rise to an NVG that should be interpreted as an MLD (Rader et al., 2015; Selway et al., 2015), and how the properties of lithospheric discontinuities vary with tectonothermal age.

Although a number of studies have previously addressed African and Arabian lithospheric structure using S-to-P receiver functions (SRFs) (Hansen et al., 2007; 2009a; 2009b; Kumar et al., 2007; Wittlinger and Farra, 2007; Savage and Silver, 2008; Dündar et al., 2011; Wölbern et al., 2012; Sodoudi et al., 2013; Mancilla et al., 2015; Liu et al., 2016), our investigation is motivated by the availability of our comprehensive new SRF database (Liu et al., 2020). No previous study has covered the entire African-Arabian region, and there are large discrepancies among previous studies as to the existence of an MLD and the depth to the LAB. For example, based on mantle xenoliths and heat-flow data, the thermal lithosphere is between 180 and 200 km thick beneath the Kalahari Craton (Artemieva and Mooney, 2001; Mather et al., 2011), whereas based on surface-wave tomography the seismic lithosphere is approximately 250-km thick (Sebai et al., 2006; Priestley et al., 2008; Pasyanos, 2010; McKenzie et al., 2015).

Here we seek new constraints on layering within the cratons by comparing previous observations of thermal age, tectonothermal history and seismic lithospheric thickness (Artemieva, 2006; Griffin et al., 2013; Pasyanos, 2010) with our new observations of the MLD. We also assess the universality of the MLD imaged beneath some other cratonic regions (again e.g the Great Plains; Liu and Gao, 2018), and we address a new controversy in which some authors have recently argued that the MLD is simply a processing artifact, a misidentification of a sidelobe resulting from the deconvolution (Kind et al., 2020) that is ubiquitous in all previous SRF studies. We only briefly discuss the LAB which seems commonly to be too gradual to be detected by body waves (e.g. Hansen et al., 2015; Liu and Gao, 2018).

2. Data, methods, and measurements

The three-component broadband teleseismic dataset utilized in the study was obtained from the Incorporated Research Institutions for Seismology (IRIS) Data Management Center (DMC) and the National Center of Earthquakes and Volcanoes within the Saudi Arabia Geological Survey (SGS) (Figure 1a). Aside from the SGS national network, the distribution is dominated by international campaign stations along the Cenozoic East African rift system, and across the mining belts of South Africa. A total of 103,878 seismograms from 9,349 teleseismic events were processed through data selection, band-pass filter, deconvolution, and move-out correction to calculate SRFs. Because SRFs typically have low signal-to-nose ratios, we binned and stacked our SRFs in circles of 1° radius, spaced on a 1° x 1° grid (Figure 2) based on piercing points calculated at 100-km depth. Detailed data, methods, and uncertainty analyses are described by Liu et al. (2020), who also present data tables of depth to and amplitude of the Moho and NVG, across Africa and Arabia. All the binned SRFs are available as west-east profiles at 1° separation with picked Moho and NVG are available as west-east profiles at 1° separation (Supplementary Material).

Our picked Moho depths vary from 15 to 67 km with an average value of 36 ± 8 km (one sigma) over our study area, and NVG depths are 50–132 km with a mean of 77 ± 13 km across the African and Arabian plates (Figures 2a, c) (Liu et al., 2020). The corresponding stacking amplitude (relative to that of the direct S-wave) is 0.05 ± 0.02 and 0.03 ± 0.02 for the Moho and NVG, respectively (Figures 2b, d). In our previous paper (Liu et al., 2020), we used a direct comparison of published P-wave receiver function (PRF) Moho depths to our SRF results to validate our SRF measurements. We also noted the lack of agreement between our SRF NVG depths and published determinations of LAB depth from surface-wave tomography, and mantle xenoliths (e.g. Pasyanos, 2010), and the spatially systematic distribution of these differences: the NVGs of stable cratons in this study (largely southern Africa) are much shallower than conventional LAB depths, whereas NVG depths are comparable to or shallower than the tomographically-determined LAB depths in tectonothermally-young regions (East African-Arabian rift system) (Figure 1b) (Liu et al., 2020). The main focus of this paper is to discuss these depths and amplitudes (Figures 2c, d), the differences from other measurements, and the relationships to tectonic setting.

2.1 The NVG is not an artifact of data processing

SRFs from cratons very commonly include a negative Sp arrival (our NVG) that follows the Moho conversion Smp and is conventionally interpreted as representing an MLD or LAB (e.g. Fischer et al., 2010; Kind et al., 2012). It has recently been questioned whether the negative arrival truly represents earth structure (i.e. an MLD or LAB) or is a sidelobe of the much stronger positive-amplitude Moho arrival (Kind et al., 2020). Such sidelobes are a well-known phenomenon associated with all filtering and deconvolution operations, including those used in the conventional SRF method (e.g. Kind et al., 2012). It has been common practice to attempt discrimination between Moho sidelobes and NVG arrivals using synthetic models (e.g. Zhao et al., 2011). More recently, the 'S-onset method' without deconvolution (intended to avoid producing sidelobes) has been used to image upper-mantle discontinuities (Kind et al., 2020). Here we follow the methodology of Liu and Gao (2018) to compare these methods and to provide confidence that in our dataset our NVG is not a processing artifact (Figures 2e, f, and 3), and should be interpreted as an MLD or LAB.

We generated 2,029 synthetic seismograms with only an S-wave positive arrival corresponding to a 35-km Moho between the crust and uppermost mantle (Figure 3a) using the Complete Ordered Ray Expansion (CORE) suite of programs (Clarke, 1993). Focal parameters (epicentral distance, focal depth, and focal mechanisms) are randomly generated in the theoretical ranges. The stacked synthetics are depth-converted using the IASP91 velocity model (Figure 3a), i.e. forming a trace equivalent to the ideal depth-converted SRF. We show the stacked synthetic seismograms without frequency filter or deconvolution (Figure 3b), without filter but with deconvolution (Figure 3c), with band-pass frequency filter (0.06–0.6 Hz) but no deconvolution (Figure 3d) corresponding to the S-onset technique, and finally processed and stacked as for our real SRFs from Africa and Arabia, i.e. with band-pass frequency filter followed by deconvolution (Figure 3e). Our deconvolution method and parameters are based on Langston (1979) and Ammon (1991). Actual data along Profile A-B (Figure 1a) processed in the same four ways are shown in Figures 3f–i.

We note that our stacked synthetics show two negative arrivals (above and below the positive Moho conversion) after filtering, whether or not deconvolution is used (Figures 3d, e), even though there is no MLD or LAB in the synthetic model (Figure 3a). The deeper negative arrival is an artifact that might be picked as an NVG. The ratios of the amplitudes of the sidelobe artifact and the Moho arrivals are 0.63 without deconvolution (Figure 3d) and 0.4 with deconvolution (Figure 3e), showing that, as intended, deconvolution reduces the influence of sidelobes. Comparison of the synthetic stack with and without filtering (0.06–0.6 Hz), with and without deconvolution (Figures 3b-e), demonstrates that the sidelobe is due to the limited band-width filter (Li et al., 2007; Zhao et al., 2011; Liu and Gao, 2018). The ratio of NVG/Moho depth is 1.9 in the synthetic trace corresponding to the S-onset method (Figure 3c) and 1.8 in the synthetic trace corresponding to a conventional SRF (Figure 3d), though these values depend on the filter parameters. The filter and deconvolution used to create Figures 3c-e are those we used to process our real data (Figures 3f-h). It is obvious that the negative pulse below the Moho positive arrival is observed whether or not deconvolution is used (Figures 3f, g).

In addition, we should expect that if the NVG on one of our real SRF stack traces is a sidelobe artifact it should have NVG/Moho amplitude ratio ~0.4, and NVG/Moho depth ratio ~1.8 (Figure 3e), recognizing that noise will modify the values seen in the synthetics. In contrast, in our actual data processed as conventional SRFs, the NVG/Moho depth ratio varies from 1.2 to > 5.0 and the NVG/Moho amplitude ratio can be as large as 5.0 (Figures 2e, f). The contrast with the S-onset-method processing is clear: note how from 5000 km to 6000 km distance, in Figure 3g without deconvolution the blue ('NVG') arrival at 50–100 km depth tracks the preceding grey

‘Moho’ arrival, rising steeply to the north to maintain a similar NVG/Moho depth ratio, whereas the same traces with deconvolution show a low-amplitude but ~uniform depth NVG (Figures 2c, 3f). For our entire dataset fewer than 25% of sample values have amplitude ratio 0.2–0.6 and depth ratio 1.4–2.2, i.e. values close to our expectation for an artifact. A sidelobe cannot be larger than the main lobe, unless quite fortuitously temporal variation of noise causes the main lobe to be diminished and/or the sidelobe to be enhanced. Observations of NVG/Moho amplitude > 1 (about 18% of our data) are therefore prima facie evidence that the NVG arrival is not an artifact, even if the amplitude ratios > 1 represent the superposition of a sidelobe on the NVG generated by true earth structure (MLD). If the sub-Moho negative arrival is the sidelobe of the Moho positive arrival, there should be a strong correlation between the Moho and the NVG depths, and between the Moho and the NVG amplitudes. We observe only small positive correlation coefficients of 0.29 and 0.39 respectively (Figure 4), perhaps evidence for superposition of the NVG with a sidelobe, but certainly providing additional evidence that the NVG represents real earth structure in many or most of our observations.

3. Discussion

3.1 Moho/NVG/LAB depths and correlation with tectonothermal age

In order to analyze the correlation between lithospheric discontinuities and tectonothermal age, we categorize the Nubia/Somalia/Arabia portion of our study area based on lithospheric age (Figures 1c, d; Artemieva, 2006; Griffin et al., 2013) and present a series of data analyses (Figures 5–10). The major limitation that we encounter is that the thermal model we use (TC1) is defined on a 1° grid, and our data are averaged over a 1°-radius circle. Inevitably, our results cannot capture abrupt tectonic boundaries or narrow transition zones that span different tectonic ages. Because of our relatively limited dataset we have grouped the nine age ranges in the TC1 model (Artemieva, 2006) to just four age ranges here (<540 Ma, 540–1100 Ma, 1100-2500 Ma, >2500 Ma) represented by 157, 306, 104 and 150 data-points respectively (Supplementary Table S1). We use all five tectonic classifications of Griffin et al. (2013) but note that the number of data in each category varies from 27 to 164 (Table S1).

3.1.1 Moho correlation between PRF and SRF data, and with tectonothermal age

Crustal thickness is more commonly measured by source-normalized P-to-S converted phases from the Moho, that is, PRFs (Langston, 1979; Zhu and Kanamori, 2000; Liu et al., 2017) than by SRFs. The number of individual SRFs is smaller than PRFs for the same seismic station distribution, due to the narrower range of useful epicentral distances, resulting in lower resolution. Nonetheless, the vast majority of Moho depths from our SRF results are similar to those from published PRFs, and have a close-to-zero mean offset irrespective of tectonic age (Figure 5d; also see Figure 4c in Liu et al. (2020) for the comparative PRF datasets). We regard this close agreement between the PRF and SRF populations as evidence of the robustness of our SRF data and analysis.

We next plot the probability density function (pdf) of SRF Moho depths as a function of age (Figure 5b) and find a striking difference between our two younger and two older age groupings. We demonstrate the statistical significance of this difference using a two-tailed t-test method (Welch, 1947), comparing the measurements of two different sized populations and variances (here, Moho depths for 0–1100 Ma and for 1100–3600 Ma lithospheric ages). The inset of Figure 5b displays the Student pdf of the two datasets, with blue vertical bars marking 95% confidence bounds: if the measured t-value of the comparison (red bar) is beyond these confidence limits, then with >95% confidence the two populations have distinct means. Figure 5b demonstrates that early Proterozoic and Archean terranes are characterized by a deeper Moho (mean 39 ± 7 km) than Phanerozoic regions (mean 32 ± 10 km), with >95% confidence, though with a large range in acceptable transition ages (850–1700 Ma, Supplementary Figures S1a-S1c). This depth difference is far too large to be accounted for by uncertainty in our assumptions of uniform (1D) P-wavespeed and V_p/V_s ratio used to compute depths from time-domain receiver functions.

We also compare our SRF measurements to the tectonothermal regionalization of Griffin et al. (2013), that assesses not only age of initial formation of the lithosphere (Archon (A), formed before 2500 Ma; Proton (P), formed 2500-1000 Ma; and Tecton (T), formed <1000 Ma), but also whether the lithospheric blocks have been significantly modified since, e.g. Archons modified in Proterozoic time (P/A) or also since 1000 Ma (T/P/A); and Protons modified since 1000 Ma (T/P) (Figures 1d, 6). (Note that Griffin et al. (2013) use a division between age groupings at 1000 Ma; Artemieva et al. (2006) instead have a boundary at 1100 Ma.) Our statistical tests are clear: Crust formed and modified only before 1000 Ma is thickest (40 ± 7 km);

and crust formed or modified since 1000 Ma is thinnest (34 ± 10 km) (Figures 6a, b). Clearly, observations of crustal-thickness differences with age – and as we show below, lithospheric-thickness difference with age – deserve to be examined further.

The assignation of age to different terranes that could affect such conclusions (e.g. Delph and Porter, 2015) seems not to be too important here. The Artemieva et al. (2006) and Griffin et al. (2013) regionalizations differ in 1/8 of cases, typically along the boundaries of well-established cratons, as to whether specific 1° bins are older or younger than these authors'1100 or 1000 Ma age boundaries. Nonetheless both regionalizations lead to very similar results (Figures 5b and 6b).

The question of whether crustal thickness changes with age has been quite controversial. The first global reviews of Precambrian crustal thickness found Archaean crust to be significantly thinner than Proterozoic crust (Durrheim and Mooney, 1991), a result seemingly in opposition to our own. Tugume et al. (2013) suggest no secular change in Moho depth in Africa and Arabia (36–45 km for Archean, 37–44 km for Archean/Paleoproterozoic, 33–40 km for Mesoproterozoic, and 38–43 km for Neoproterozoic), but did not statistically test their results. In contrast, in southern Africa Stankiewicz and de Wit (2013) find "a general decrease in depth to Moho towards the present" for crust dated from 3.6–0.1 Ga, but they emphasize the large variability within each age group that we also find in our data. Significant differences between the different compilations certainly arise in the choice of datasets, as well as, potentially, in the assignation of age to different terranes (e.g. Delph and Porter, 2015).

Durrheim & Mooney (1991), Tugume et al. (2013) and Stankiewicz & de Wit (2013) all focus on crustal thickness as a function of surface age, rather than, as here, tectonothermal age (Artemieva, 2006) or age of most recent "re-working" (Griffin et al., 2013). It is important to note that none of these compilations strictly tests for secular change in the thickness of crust at its formation, despite attempts to draw such inferences. Rather, we are testing for secular change in the final crustal thickness that results from formation and all subsequent tectonic events, potentially including both thinning and thickening. Our clear conclusion is that for the Arabia-Somali-Nubia plates as sampled by us, a change in Earth processes has led to preservation of systematically thinner crust since the Meso- or Neoproterozoic. These tectonothermally younger and thinner regions include both classic areas of Cenozoic rifting (African-Arabian rift system) as well as regions formed by Neoproterozoic continental collision, albeit followed by orogenic collapse (e.g. East Africa-Antarctic orogen) (Begg et al., 2009; Stern & Johnson, 2010).

Despite the significant change in crustal thickness between Archean and Phanerozoic crust, we found no simple monotonic trend with time. Statistically, our dataset shows similar crustal thickness for all terranes unmodified since 1100 Ma (Archaean and older Proterozoic); and also similar thicknesses for all terranes younger than or reworked since 1100 Ma (Phanerozoic and Neoproterozoic) (Figure 5a). Elsewhere in the world it has been suggested, though without statistical verification, that younger Archean terranes are thicker than older ones (Abbott et al., 2013; Yuan, 2015). Figures 5a and 6a hint that Meso-to-Paleoproterozoic crust and Protons could be marginally thicker than Archean crust and Archons, but the difference is not significant.

In contrast to the clear crustal-thickness change, Moho conversion amplitude, which we take as a proxy for the wavespeed contrast across the Moho, has no obvious correlation between TC1 tectonothermal age (Figure 5c), and only a hint of stronger Moho amplitudes beneath Archons (Figure 6c) that is not statistically significant (Figure 6d). We suggest this lack of secular trend arises because wavespeed contrast across the Moho depends on many evolutionary aspects, such as diking/underplating of mantle material that would lower the contrast and lower-crustal delamination that would increase the contrast (e.g. Liu and Gao, 2010), so that in any individual area Moho amplitude may change over time. Abbott et al. (2013) proposed that pristine Archean cratons are characterized by a sharp (abrupt, not gradational) Moho, but SRFs are not ideal to measure Moho sharpness because their frequency is lower than PRFs, and sharpness is not necessarily well-correlated with the amplitude measurements that we present here.

3.1.2 LAB correlation with tectonothermal age

In simple thermal models of the lithosphere, LAB depth increases with tectonothermal age due to conductive cooling. Global model TC1 (Figure 7c; Artemieva, 2006) indeed shows a monotonic increase in lithospheric thickness with age, but this reflects the method used to estimate LAB depth from terrane age in regions lacking robust surface heat-flow measurements. However, there is also a statistically significant correlation between age of terranes in model TC1 and lithospheric thickness as estimated from seismic tomography (Pasyanos, 2010: model

LITHO_1.0), with older lithosphere being thicker (Figure 7a). The separation into two fields is clearest if we split our dataset at 1100 Ma (Figure 7b), though as for crustal thickness the statistical difference is present whether we break the dataset at 850, 1100 or 1700 Ma (Supplementary Figure S1d-S1f). Just as for measurements of crustal thickness (Figures 5a, b), some outliers with very shallow LAB appear within ancient cratons (Figure 7a), likely due to our relatively coarse 1°-radius bins averaging thin lithosphere of adjacent margins and rifts into a craton measurement. The converse is also true with occasional measurements of surprisingly large crustal and lithospheric thickness in young terranes adjacent to cratons. This increase of seismic lithosphere thickness with age seems to be model independent as it is also well-displayed in the 2°-resolution CAM_2016 global model (Ho et al., 2016) (Supplementary Figure S2). The Begg et al. (2009) and Griffin et al. (2013) regionalizations are likely somewhat subjective, as the authors describe defining boundaries using topographic, geologic, geochronometric, gravity, and magnetic data and their seismic tomography results. Because their model construction includes tomographic results, and presuming that Begg et al. (2009) and Griffin et al. (2013) assumed thicker lithosphere is older lithosphere, we find as expected that purely seismic models (Pasyanos, 2010; Ho et al., 2016) show thinnest lithosphere beneath Tectons, and thicker lithosphere beneath Protons and Archons, just as for the Artemieva (2006) TC1 model (Supplementary Figure S2).

3.1.3 NVG correlation with tectonothermal age

In contrast to the LAB and Moho depths, we find no visual correlation between our NVG depth and TC1 thermal age (Figures 8a, b), and a barely significant change for the Griffin et al. (2013) regionalization (Figures 9a, b). The lack of secular depth change is further shown by plots of the difference between NVG and LAB depth as a function of age (Figures 7b, d) that qualitatively resemble plots of lithospheric thickness as a function of age (Figures 7a, c), and by the lack of correlation between our NVG and the age-dependent seismic/thermal LAB depths (correlation coefficients 0.07 and 0.06, respectively: Figure S3). However, the mean conversion amplitude of the NVG has a weak positive association both with TC1 thermal age (Figures 8c, d), ~10% higher amplitude for 1100–3600 Ma lithosphere than for younger lithosphere (0–1100 Ma), and with the Griffin et al. (2013) ages (Figures 9c, d), ~20% higher amplitude for Archons than for younger or reworked lithosphere.

Both the measured depth to and amplitude of the NVG depend on the method used to determine them. Our preferred method to identify the depth and amplitude of the NVG combines a bootstrap method with manual inspection and necessary adjustment of the selected peak if multiple peaks are present on a trace (Liu et al., 2020). In Figure S4 we compare our preferred NVG depths to depths determined entirely by an automatic search in the depth range of 50-150 km. We find effectively identical results for ~60% of bins (values within <10 km) (Figure S4a), and that there is negligible bias introduced with age (Figure S4b). Probability-distribution functions of NVG depth and amplitude derived by 'manual' (Figures 8, 9) and 'automatic' methods (Figure S5) are very similar, but more tightly focused (smaller variance) using the bootstrap/manual method.

3.2 Implications for nature of MLD and LAB

Our NVG depths have large discrepancies with both thermal predictions and tomographic measurements of lithospheric thickness, except for the youngest ages, and the mean discrepancies exceed 100 km for Paleoproterozoic and Archean cratons (Figures 1b, 7b, 7d). NVG depths for <1100 Ma lithosphere are close to the mean tomographic LAB depth of the same age (Figures 7b, 10b): the tomographic LAB averages only 18 km deeper than the NVG, but the LAB standard deviation is >60 km for LITHO_1.0 (Pasyanos, 2010) (14 km deeper and >40 km deviation for CAM_2016 (Figure S2; Ho et al., 2016)). The NVG depths match thermal LAB depths very well for Phanerozoic (0–540 Ma) crust (Figures 7d, 10a), allowing the possibility that the NVG represents LAB beneath rifts and margins. We do not show t-tests in these cases because both the 'young' thermal and tomographic LABs appear to have bimodal distributions (Figure 10). In contrast, the NVG is clearly much shallower (50–150 km on average) than both the tomographic and the thermal LAB in Meso- and Paleoproterozic and Archean terranes (Figures 7b, d). This similarity of NVG and tomographic LAB for Neoproterozoic terranes <1100 Ma could be interpreted as representing a very slow thickening of lithosphere over a billion, not hundreds of millions, of years (thermal time constant of 100-km thick lithosphere (thickness squared divided by thermal diffusivity) is ~1000 Ma). Alternatively, some regions shown by model TC1 as Neoproterozoic (Figure 1c; Artemieva, 2006) have likely been extensively thermally reactivated (Figure 1d), including in the Neogene to produce a significant population of points in our database with nominally Neoproterozoic lithosphere <100 km thick (Arabian shield: Blanchette et al., 2018; Ethiopian plateau: Keranen et al., 2009).

The most important conclusion of these comparisons, given our demonstration that the NVG is not a processing artifact, is that the 50–150 km separation between NVG and LAB in Meso- and Paleoproterozoic and Archean cratons (Figures 1c, 7) requires the existence of an MLD as a geologic feature distinct from the LAB. The relative NVG stacking amplitudes of 0.025–0.035 corresponding to the LAB in rifts and margins of the study area (Figures 8c, d) are comparable to those observed beneath the tectonically active western U.S. (Liu and Gao, 2018). In contrast, the average NVG amplitude of 0.033 corresponding to an MLD in Meso- and Paleoproterozoic and Archean cratons (Figures 8c, d) is apparently higher than that beneath the stable cratonic region of the central U.S. (~0.01). In contrast to the relatively-well understood LAB, the formation mechanism of an MLD is still strongly debated. The weak or absent correlation between NVG depth and tectonothermal age indicates that the MLD does not evolve with increasing lithospheric age as a thermal boundary, supporting the hypothesis that the MLD is a compositionally distinct layer rich in seismically slow minerals (phlogopite/amphibole) (Rader et al., 2015; Selway et al., 2015). The MLD might form at or close to the LAB during lithospheric thinning, as suggested by the equivalence of NVG and LAB depths in actively or recently rifted regions (Figures 7, 10), perhaps by magmas trapped at that depth. The MLD would then remain frozen in place as the lithosphere thickens by cooling. Our possible evidence of increasing NVG amplitude with lithospheric age (Figures 8d, 9d) is consistent with the gradual growth of such a layer over time, if it traps small melt fractions (McKenzie, 1989).

4. Conclusions

Previous investigations of lithospheric discontinuities within Africa and Saudi Arabia have been either low-resolution, highly localized, or sparse. Our comprehensive SRF analysis provides new constraints on the depths of lithospheric discontinuities, and their associations with tectonothermal ages, by filling the data gap using the IRIS and SGS seismic arrays. Our analyses lead to the following conclusions:

1. Comparing our conventional SRF processing with recent S-onset methods (Liu and Gao, 2018; Kind et al., 2020) using real and synthetic dataset, respectively, we conclude that the NVG beneath the Moho is not an artifact of data processing, and must represent an MLD or the LAB.
2. In tectonically active and recently active areas (Phanerozoic and Neoproterozoic), the NVG represents the sharp discontinuity between the rigid lithospheric plate and weaker asthenosphere. Beneath African cratons (largely represented in our database by the Tanzania and Kalahari cratons), the NVG is a low-wavespeed MLD, sharper than has been observed beneath the central U.S.
3. Phanerozoic and Neoproterozoic tectonic processes have preserved thinner continental crust than Archean and Paleoproterozoic processes, in Western Gondwana.

Acknowledgements

We thank Irina Artemieva and Graham Begg for sharing details of their tectonothermal models of Africa; and Chris Castillo for GIS assistance.

References

Abbott, D. H., Mooney, W. D., & VanTongeren, J. A. (2013). The character of the Moho and lower crust within Archean cratons and the tectonic implications. Tectonophysics, 609, 690-705.

Abdelsalam, M. G., Liégeois, J. P., & Stern, R. J. (2002). The Saharan metacraton. Journal of African Earth Sciences, 34(3-4), 119-136.

Abt, D. L., Fischer, K. M., French, S. W., Ford, H. A., Yuan, H., & Romanowicz, B. (2010). North American lithospheric discontinuity structure imaged by Ps and Sp receiver functions. Journal of Geophysical Research: Solid Earth, 115(B9).

Ammon, C. J. (1991). The isolation of receiver effects from teleseismic P waveforms. Bulletin of the seismological Society of America, 81(6), 2504-2510.

Artemieva, I. M., & Mooney, W. D. (2001). Thermal thickness and evolution of Precambrian lithosphere: A global study. Journal of Geophysical Research: Solid Earth, 106(B8), 16387-16414.

Artemieva, I. M. (2006). Global 1× 1 thermal model TC1 for the continental lithosphere: implications for lithosphere secular evolution. Tectonophysics, 416(1-4), 245-277.

Artemieva, I. M. (2009). The continental lithosphere: reconciling thermal, seismic, and petrologic data. Lithos, 109(1-2), 23-46.

Artemieva, I. (2011). Lithosphere: an interdisciplinary approach. Cambridge University Press.

Aulbach, S., Massuyeau, M., & Gaillard, F. (2017). Origins of cratonic mantle discontinuities: A view from petrology, geochemistry and thermodynamic models. Lithos, 268, 364-382.

Begg, G. C., Griffin, W. L., Natapov, L. M., O'Reilly, S. Y., Grand, S. P., O'Neill, C. J., Hronsky, J. M. A., Djomani, Y. P., Swain, C. J., Deen, T. & Bowden, P. (2009). The lithospheric architecture of Africa: Seismic tomography, mantle petrology, and tectonic evolution. Geosphere, 5(1), 23-50.

Blanchette, A. R., Klemperer, S. L., Mooney, W. D., & Zahran, H. M. (2018). Two-stage Red Sea rifting inferred from mantle earthquakes in Neoproterozoic lithosphere. Earth and Planetary Science Letters, 497, 92-101.

Camp, V. E., & Roobol, M. J. (1992). Upwelling asthenosphere beneath western Arabia and its regional implications. Journal of Geophysical Research: Solid Earth, 97(B11), 15255-15271. doi:10 .1029 /92JB00943.

Clarke, T. J. (1993). The complete ordered ray expansion—II. Multiphase body wave tomography. Geophysical Journal International, 115(2), 435-444.

Delph, J. R., & Porter, R. C. (2015). Crustal structure beneath southern Africa: insight into how tectonic events affect the Mohorovičić discontinuity. Geophysical Journal International, 200(1), 254-264.

Dündar, S., Kind, R., Yuan, X., Bulut, F., Sodoudi, F., Heit, B., Kumar, P., Li, X., Hanka, W., Martin, R. and Stiller, M. (2011). Receiver function images of the base of the lithosphere in the Alboran Sea region. Geophysical Journal International, 187(2), 1019-1026.

Durrheim, R. J., & Mooney, W. D. (1991). Archean and Proterozoic crustal evolution: Evidence from crustal seismology. Geology, 19(6), 606-609.

Faul, U. H., & Jackson, I. (2005). The seismological signature of temperature and grain size variations in the upper mantle. Earth and Planetary Science Letters, 234(1-2), 119-134.

Fay, M. P., & Proschan, M. A. (2010). Wilcoxon-Mann-Whitney or t-test? On assumptions for hypothesis tests and multiple interpretations of decision rules. Statistics surveys, 4, 1.

Fischer, K. M., Ford, H. A., Abt, D. L., & Rychert, C. A. (2010). The lithosphere-asthenosphere boundary. Annual Review of Earth and Planetary Sciences, 38, 551-575. 10.1146/annurev-earth-040809-152438

Gholamrezaie, E., Scheck-Wenderoth, M., Sippel, J., & Strecker, M. R. (2018). Variability of the geothermal gradient across two differently aged magma-rich continental rifted margins of the Atlantic Ocean: the Southwest African and the Norwegian margins. Solid Earth, 9(1).

Globig, J., Fernàndez, M., Torne, M., Vergés, J., Robert, A., & Faccenna, C. (2016). New insights into the crust and lithospheric mantle structure of Africa from elevation, geoid, and thermal analysis. Journal of Geophysical Research: Solid Earth, 121(7), 5389-5424.

Griffin, W., Begg, G. & O'Reilly, S. (2013). Continental-root control on the genesis of magmatic ore deposits. Nature Geoscience, 6, 905–910.

Hansen, S. E., Nyblade, A. A., and Julia, J. (2009a). Estimates of crustal and lithospheric thickness in Sub-Saharan Africa from S-wave receiver functions. South African Journal of Geology, 112(3-4), 229-240.

Hansen, S. E., Nyblade, A. A., Julia, J., Dirks, P. H., and Durrheim, R. J. (2009b). Upper-mantle low-velocity zone structure beneath the Kaapvaal craton from S-wave receiver functions. Geophysical Journal International,178(2), 1021-1027.

Hansen, S. E., Rodgers, A. J., Schwartz, S. Y., and Al-Amri, A. M. (2007). Imaging ruptured lithosphere beneath the Red Sea and Arabian Peninsula. Earth and Planetary Science Letters, 259(3-4), 256-265.

Hansen, S. M., Dueker, K., and Schmandt, B. (2015). Thermal classification of lithospheric discontinuities beneath USArray. Earth and Planetary Science Letters, 431, 36-47.

Ho, T., Priestley, K., & Debayle, E. (2016). A global horizontal shear velocity model of the upper mantle from multimode Love wave measurements. Geophysical journal international, 207(1), 542-561.

Karato, S. I., & Park, J. (2018). On the origin of the upper mantle seismic discontinuities. Lithospheric Discontinuities, 5-34.

Keranen, K. M., Klemperer, S. L., Julia, J., Lawrence, J. F., & Nyblade, A. A. (2009). Low lower crustal velocity across Ethiopia: Is the Main Ethiopian Rift a narrow rift in a hot craton?. Geochemistry, Geophysics, Geosystems, 10(5).

Kind, R., Mooney, W. D., & Yuan, X. (2020). New insights into the structural elements of the upper mantle beneath the contiguous United States from S-to-P converted seismic waves. Geophysical Journal International, 222(1), 646-659.

Kind, R., Yuan, X., & Kumar, P. (2012). Seismic receiver functions and the lithosphere–asthenosphere boundary. Tectonophysics, 536, 25-43.

King, S. D., & Ritsema, J. (2000). African hot spot volcanism: small-scale convection in the upper mantle beneath cratons. Science, 290(5494), 1137-1140.

Korenaga, J., & H. Jordan, T. (2002). On the state of sublithospheric upper mantle beneath a supercontinent. Geophysical Journal International, 149(1), 179-189.

Kumar, P., Yuan, X., Kumar, M. R., Kind, R., Li, X., and Chadha, R. K. (2007). The rapid drift of the Indian tectonic plate. Nature, 449(7164), 894.

Langston, C. A. (1979). Structure under Mount Rainier, Washington, inferred from teleseismic body waves. Journal of Geophysical Research: Solid Earth, 84(B9), 4749-4762.

Li, X., Yuan, X., & Kind, R. (2007). The lithosphere-asthenosphere boundary beneath the western United States. Geophysical Journal International, 170(2), 700-710.

Liu, K. H., & Gao, S. S. (2010). Spatial variations of crustal characteristics beneath the Hoggar swell, Algeria, revealed by systematic analyses of receiver functions from a single seismic station. Geochemistry, Geophysics, Geosystems, 11(8).

Liu, L., and Gao, S. S. (2018). Lithospheric layering beneath the contiguous United States constrained by S-to-P receiver functions. Earth and Planetary Science Letters, 495, 79-86.

Liu, L., Gao, S. S., Liu, K. H., and Mickus, K. (2017). Receiver function and gravity constraints on crustal structure and vertical movements of the Upper Mississippi Embayment and Ozark Uplift. Journal of Geophysical Research: Solid Earth, 122(6), 4572-4583.

Liu, L., Liu, K. H., & Gao, S. S. (2016, December). Lithospheric layering beneath southern Africa constrained by S-to-P receiver functions. In AGU Fall Meeting Abstracts.

Liu, L., Tong, S., Li, S., & Qaysi, S. (2020). Sp Receiver-Function Images of African and Arabian Lithosphere: Survey of Newly Available Broadband Data. Seismological Research Letters, 91(3), 1813-1819.

Mancilla, F. D. L., Stich, D., Morales, J., Martín, R., Diaz, J., Pazos, A., ... and Gonzalez-Lodeiro, F. (2015). Crustal thickness and images of the lithospheric discontinuities in the Gibraltar arc and surrounding areas. Geophysical Supplements to the Monthly Notices of the Royal Astronomical Society, 203(3), 1804-1820.

Mann, H. B., & Whitney, D. R. (1947). On a test of whether one of two random variables is stochastically larger than the other. Annals of Mathematical Statistics, 50-60.

Mather, K. A., Pearson, D. G., McKenzie, D., Kjarsgaard, B. A., & Priestley, K. (2011). Constraints on the depth and thermal history of cratonic lithosphere from peridotite xenoliths, xenocrysts and seismology. Lithos, 125(1-2), 729-742.

McKenzie, D. (1989). Some remarks on the movement of small melt fractions in the mantle. Earth and planetary science letters, 95(1-2), 53-72.

McKenzie, D., Daly, M. C., & Priestley, K. (2015). The lithospheric structure of Pangea. Geology, 43(9), 783-786.

Pasyanos, M. E. (2010). Lithospheric thickness modeled from long-period surface wave dispersion. Tectonophysics, 481(1-4), 38-50.

Priestley, K., McKenzie, D., Debayle, E., & Pilidou, S. (2008). The African upper mantle and its relationship to tectonics and surface geology. Geophysical Journal International, 175(3), 1108-1126.

Rader, E., Emry, E., Schmerr, N., Frost, D., Cheng, C., Menard, J., Yu, C.Q. & Geist, D. (2015). Characterization and petrological constraints of the midlithospheric discontinuity. Geochemistry, Geophysics, Geosystems, 16(10), 3484-3504.

Rychert, C. A., Harmon, N., Constable, S., & Wang, S. (2020). The Nature of the Lithosphere-Asthenosphere Boundary. Journal of Geophysical Research: Solid Earth, 125(10), e2018JB016463.

Savage, B., & Silver, P.G. (2008). Evidence for a compositional boundary within the lithospheric mantle beneath the Kalahari craton from S receiver functions. Earth and Planetary Science Letters, 272(3-4), 600-609.

Sebai, A., Stutzmann, E., Montagner, J. P., Sicilia, D., & Beucler, E. (2006). Anisotropic structure of the African upper mantle from Rayleigh and Love wave tomography. Physics of the Earth and Planetary Interiors, 155(1-2), 48-62.

Selway, K., Ford, H., & Kelemen, P. (2015). The seismic mid-lithosphere discontinuity. Earth and Planetary Science Letters, 414, 45-57.

Sodoudi, F., Yuan, X., Kind, R., Lebedev, S., Adam, J. M. C., Kästle, E., and Tilmann, F. (2013). Seismic evidence for stratification in composition and anisotropic fabric within the thick lithosphere of Kalahari Craton. Geochemistry, Geophysics, Geosystems, 14(12), 5393-5412.

Stankiewicz, J., & de Wit, M. (2013). 3.5 billion years of reshaped Moho, southern Africa. Tectonophysics, 609, 675-689.

Stern, R. J., & Johnson, P. (2010). Continental lithosphere of the Arabian Plate: a geologic, petrologic, and geophysical synthesis. Earth-Science Reviews, 101(1-2), 29-67.

Thybo, H. (2006). The heterogeneous upper mantle low velocity zone. Tectonophysics, 416(1-4), 53-79.

Thybo, H., & Perchuć, E. (1997). The seismic 8 discontinuity and partial melting in continental mantle. Science, 275(5306), 1626-1629.

Tugume, F., Nyblade, A., Julià, J., & van der Meijde, M. (2013). Precambrian crustal structure in Africa and Arabia: evidence lacking for secular variation. Tectonophysics, 609, 250-266.

Welch, B. L. (1947). The generalization of students' problem when several different population variances are involved. Biometrika, 34(1/2), 28-35.

Wittlinger, G., and Farra, V. (2007). Converted waves reveal a thick and layered tectosphere beneath the Kalahari super-craton. Earth and Planetary Science Letters, 254(3-4), 404-415.

Wölbern, I., Rümpker, G., Link, K., and Sodoudi, F. (2012). Melt infiltration of the lower lithosphere beneath the Tanzania craton and the Albertine rift inferred from S receiver functions. Geochemistry, Geophysics, Geosystems, 13(8).

Yuan, H. (2015). Secular change in Archaean crust formation recorded in Western Australia. Nature Geoscience, 8(10), 808-813.

Zhao, W., Kumar, P., Mechie, J., Kind, R., Meissner, R., Wu, Z., Shi, D., Su, H., Xue, G., Karplus, M. and Tilmann, F., 2011. Tibetan plate overriding the Asian plate in central and northern Tibet. Nature geoscience, 4(12), 870-873.

Zhu, L., and Kanamori, H. (2000). Moho depth variation in southern California from teleseismic receiver functions. Journal of Geophysical Research: Solid Earth, 105 (B2), 2969–2980. https:// doi.org/10.1029/1999JB900322.

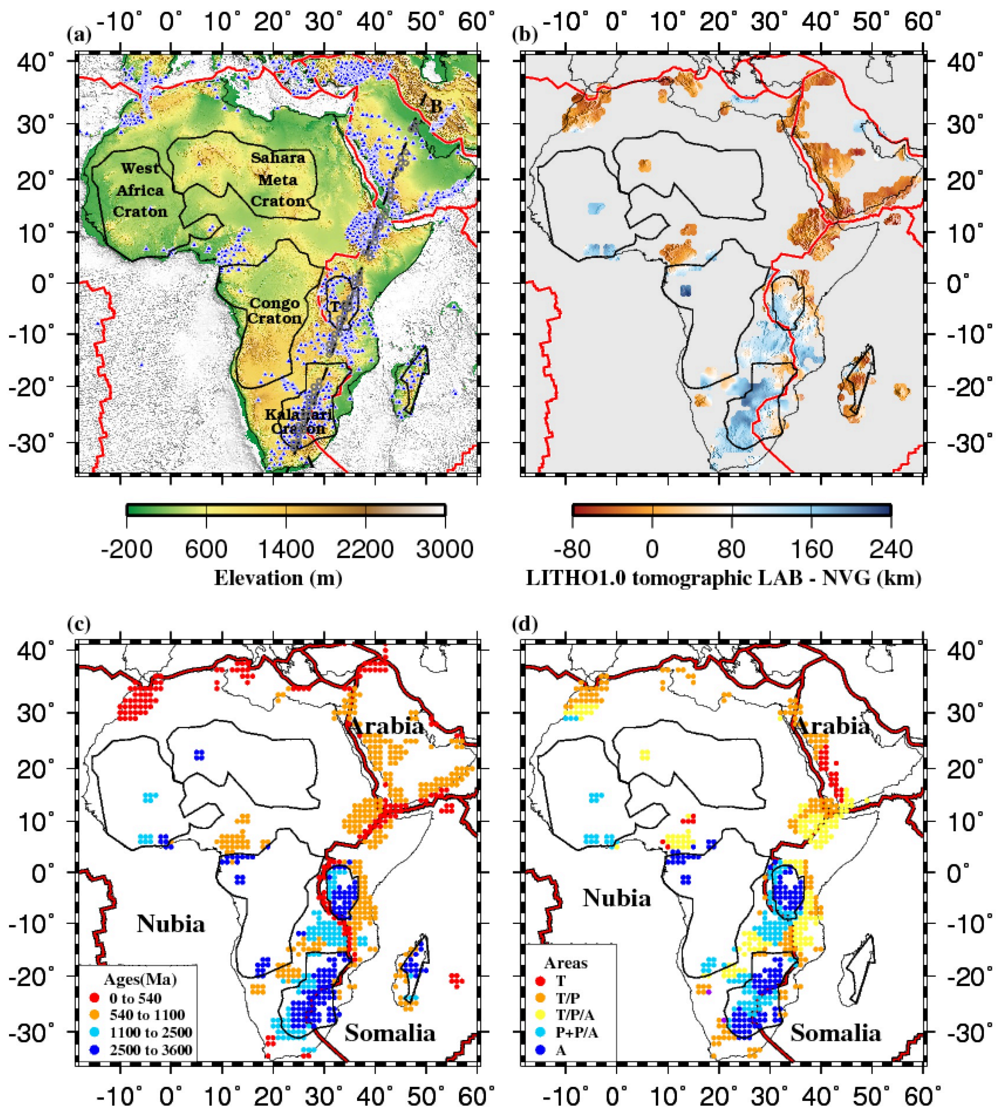

Figure 1. (a) Topographic relief map of our database area (Liu et al., 2020) showing seismic stations (blue triangles; of stations on the European plate only those adjacent to the plate boundary contribute to the bins studied in this paper), plate boundaries (red lines after Bird, 2003), and the major Archean & Paleoproterozoic shields & platforms (solid black lines; TC=Tanzania craton). Black dashed line A-B is cross-section, and grey open circles the SRF traces, shown in Figure 3. Craton boundaries are plotted based on a 1700 Ma cut-off between craton and non-craton, following Artemieva (2006). (b) Difference between published tomographically-inferred lithospheric thickness (LITHO_1.0; Pasyanos, 2010) and the depth of NVG obtained from our SRF measurements (blue color where LAB deeper than NVG). (c) Tectonic ages of the African and Arabian continents on a 1° × 1° grid from the 'TC1' thermal model for the continental lithosphere (Artemieva, 2006). (d) Tectonothermal regionalization of Begg et al. (2009) updated by Griffin et al. (2013): Archon (A), formed before 2500 Ma; Proton (P), formed 2500-1000 Ma; Tecton (T), formed <1000 Ma), Archons significantly modified in Proterozoic time (P/A) or also since 1000 Ma (T/P/A); and Protons significantly modified since 1000 Ma (T/P). In parts c and d, ages are shown only where we report SRF data.

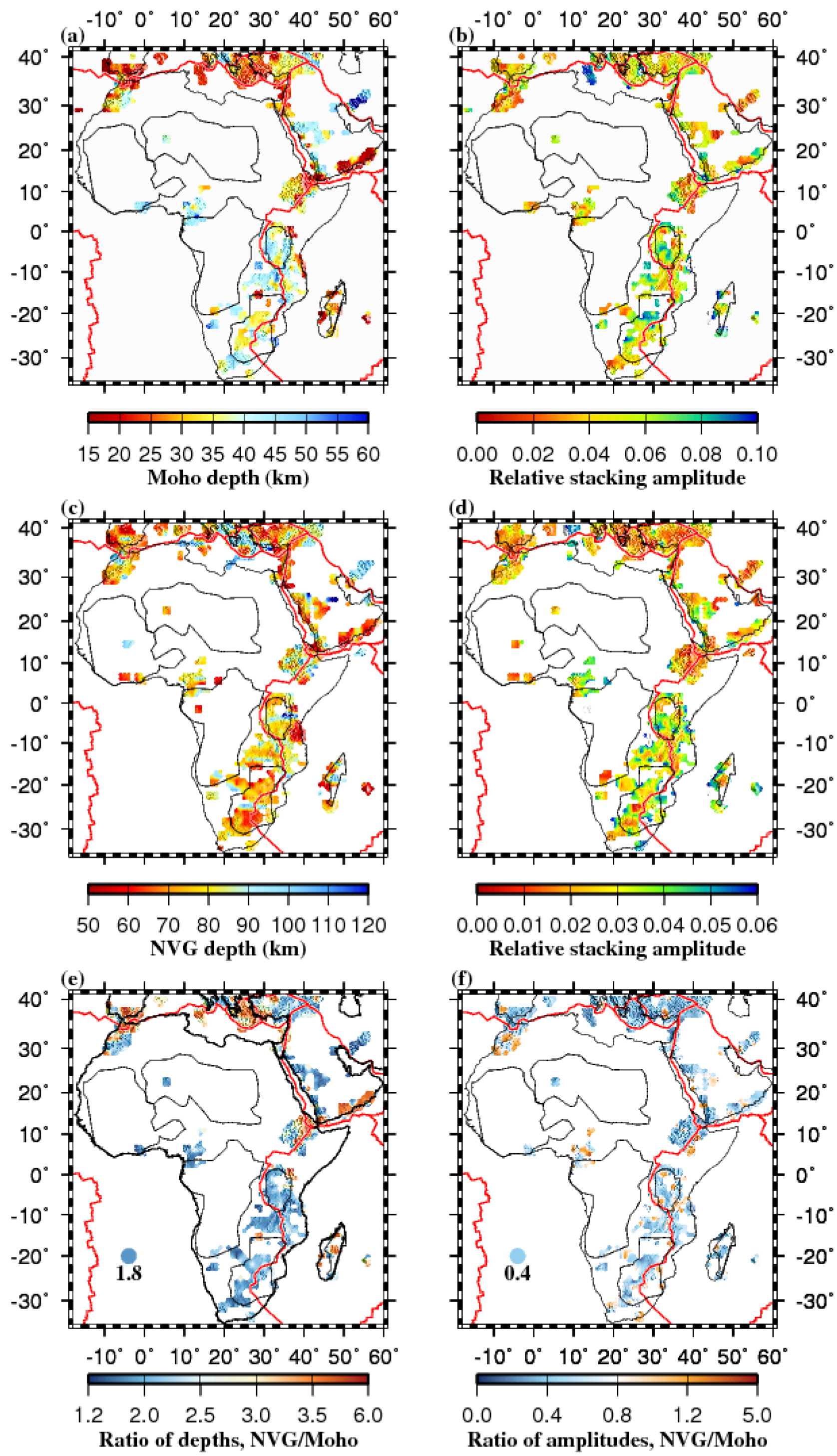

Figure 2. (a) SRF depth for the Moho. (b) SRF Moho stacking amplitude (relative to that of the direct S-wave). (c) SRF depth of the negative velocity gradient (NVG). (b) SRF NVG stacking amplitude (relative to direct S). (e) Ratio of depths of the NVG and the Moho. (f) Ratio of stacking amplitudes of the NVG and the Moho. Colored circles in bottom left of (e) and (f) are those of the NVG/Moho depth ratio and amplitude ratio of our synthetic stack Figure 3e.

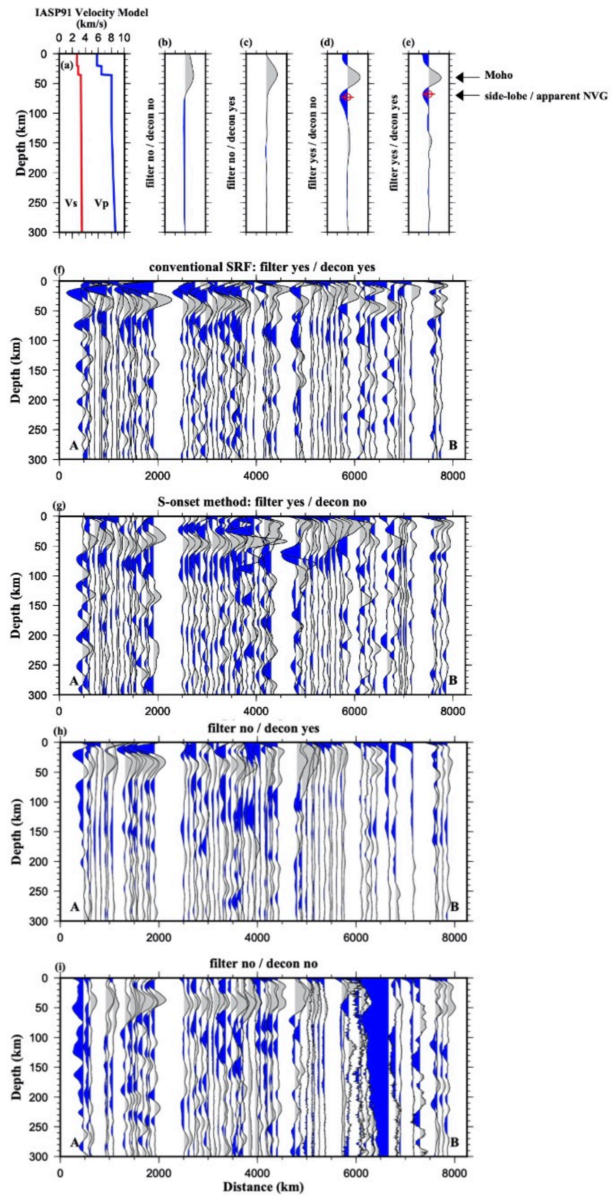

Figure 3. (a) V(z) model from IASP91 Earth model (Kennett and Engdahl, 1991). (b) Depth series from 2,029 CORE synthetic seismograms without filter and deconvolution. (c) same as (b) but with deconvolution and without filter. (d) same as (b) but with filter and without deconvolution. (e) same as (b) but with filter and deconvolution. The red circles in the depth range of 60-150 km represent picked depths of the NVG, including in parts d and e where the circles represent an artifact. (f) Observed depth series along profile A-B in Figure 1a using band-pass filter and deconvolution. (g) Same as (f) but without deconvolution. (h) Same as (f) but without filter. (i) Same as (f) but without filter and deconvolution. Data in (f-i) were automatically processed, so generating output traces even for 1°-bins where manual inspection and comparison of traces failed to produce an NVG image. The same data processed with manual inspection are shown as Figure 3b of Liu et al. (2020). Picks of Moho and NVG on these data are available in the on-line data repository, see Supplementary Material.

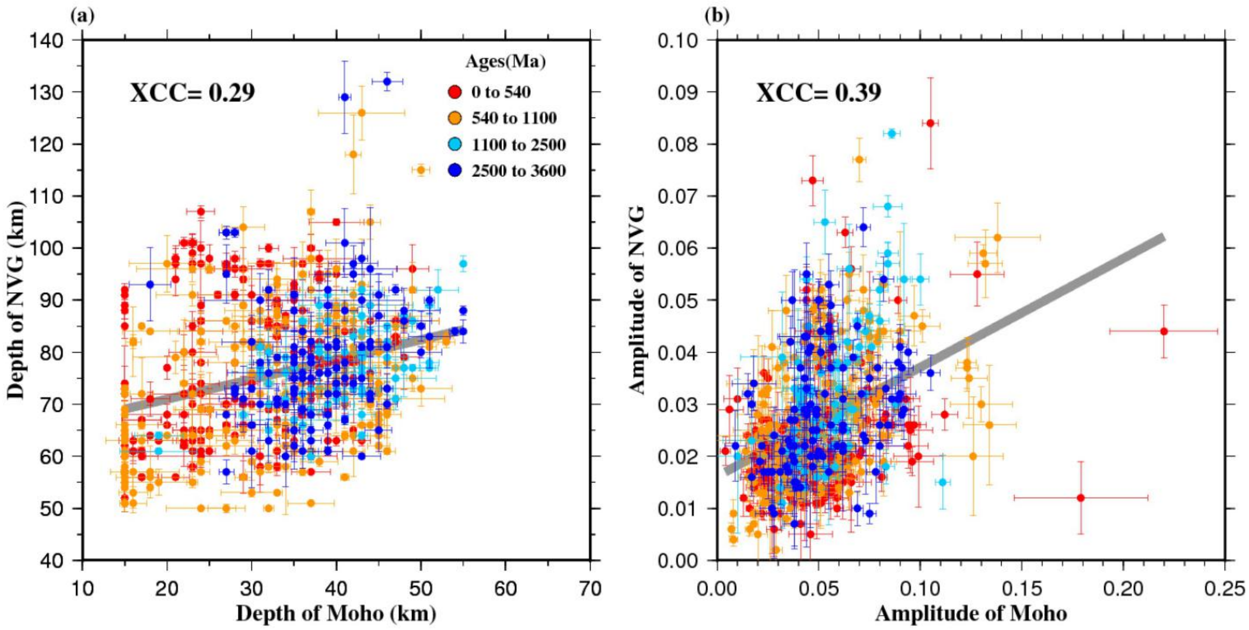

Figure 4. (a) NVG depth plotted against Moho depth for Nubia/Somalia/Arabia. (b) NVG amplitude plotted against Moho amplitude. XCC: cross-correlation coefficient. The colors of circles are those of the 'TC1' thermal model in Figure 1c.

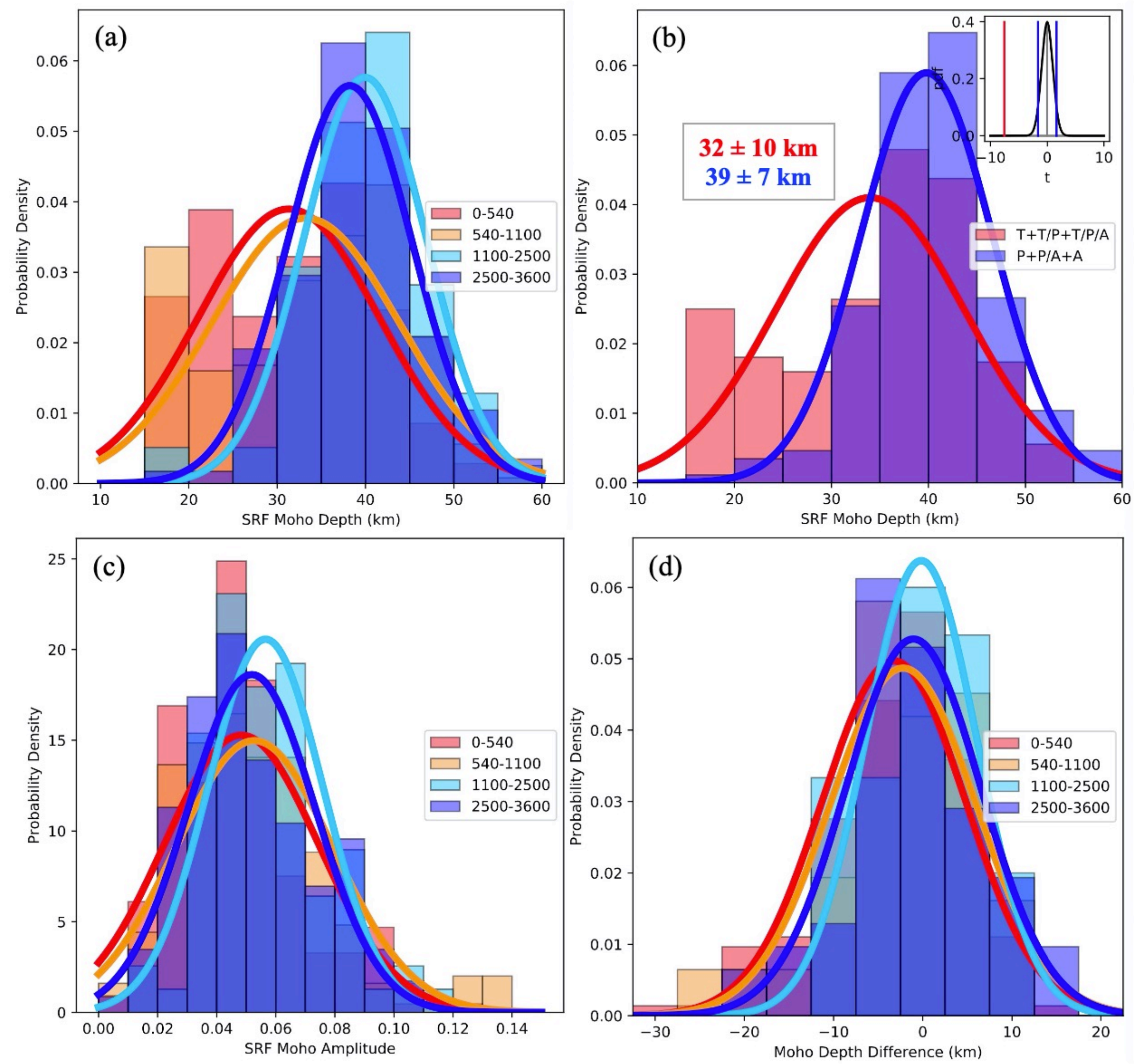

Figure 5. SRF-Moho statistics for Nubia/Somalia/Arabia. Relative histograms of (a and b) Moho depths, (c) relative stacking amplitudes corresponding to the Moho and (d) difference between our Sp and published Ps measurements for Moho (SRF minus PRF). (a), (c) and (d) are organized by thermal ages (0–540, 540–1100, 1100–2500 and 2500–3600 Ma); in (b) ages are grouped into 0–1100 Ma and 1100–3600 Ma. Gaussian curves in the foreground are best-fit relative probability density functions of each category. The colors of bars, curves and lettering are as in the ‘TC1’ thermal model in Figure 1c (except in b where red and blue represent young and ancient. In (b), our comparison of young and ancient regions, the means and standard deviations for the two categories are shown (colored lettering in boxes); upper-right inset is the t-test, showing the two populations appear statistically quite distinct.

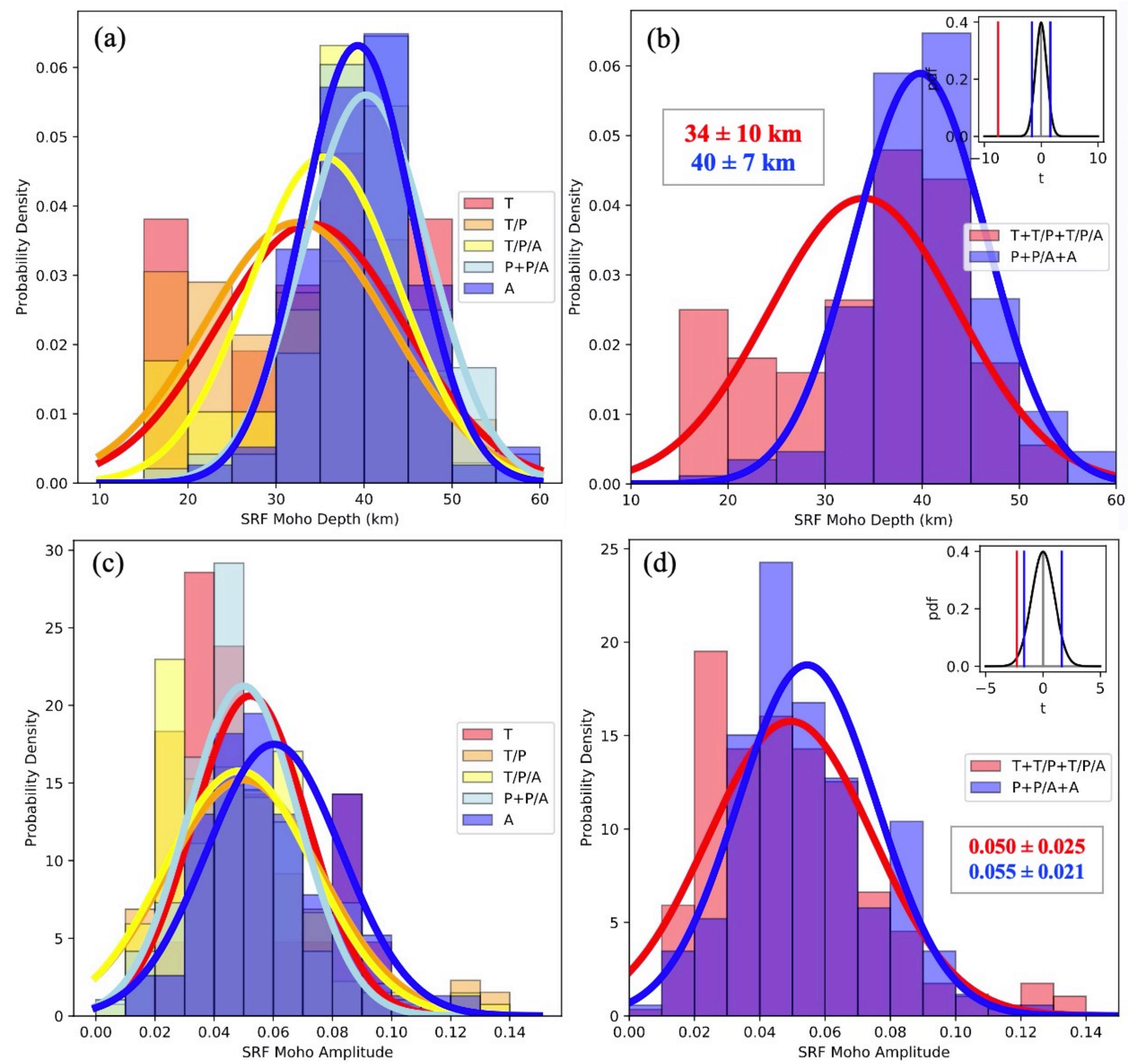

Figure 6. SRF-Moho statistics for Nubia/Somalia/Arabia, plotted as in Figure 5. Histograms of (a and b) Moho depths, (c and d) Moho conversion amplitude, divided following Griffin et al. (2013) into Archons (A), Protons (P), Tectons (T), Archons significantly reworked in Proterozoic time (P/A), or also since 1000 Ma (T/P/A), and Protons reworked since 1000 Ma (T/P). The colors of bars, curves and lettering in (a) and (c) are as in the Griffin et al. (2013) regionalization in Figure 1d; in part (b) and (d) are red (T+T/P+T/P/A) and dark blue (P+P/A+A). T-tests in (b) and (d) show t-values for T+T/P+T/P/A compared to P+P/A+A.

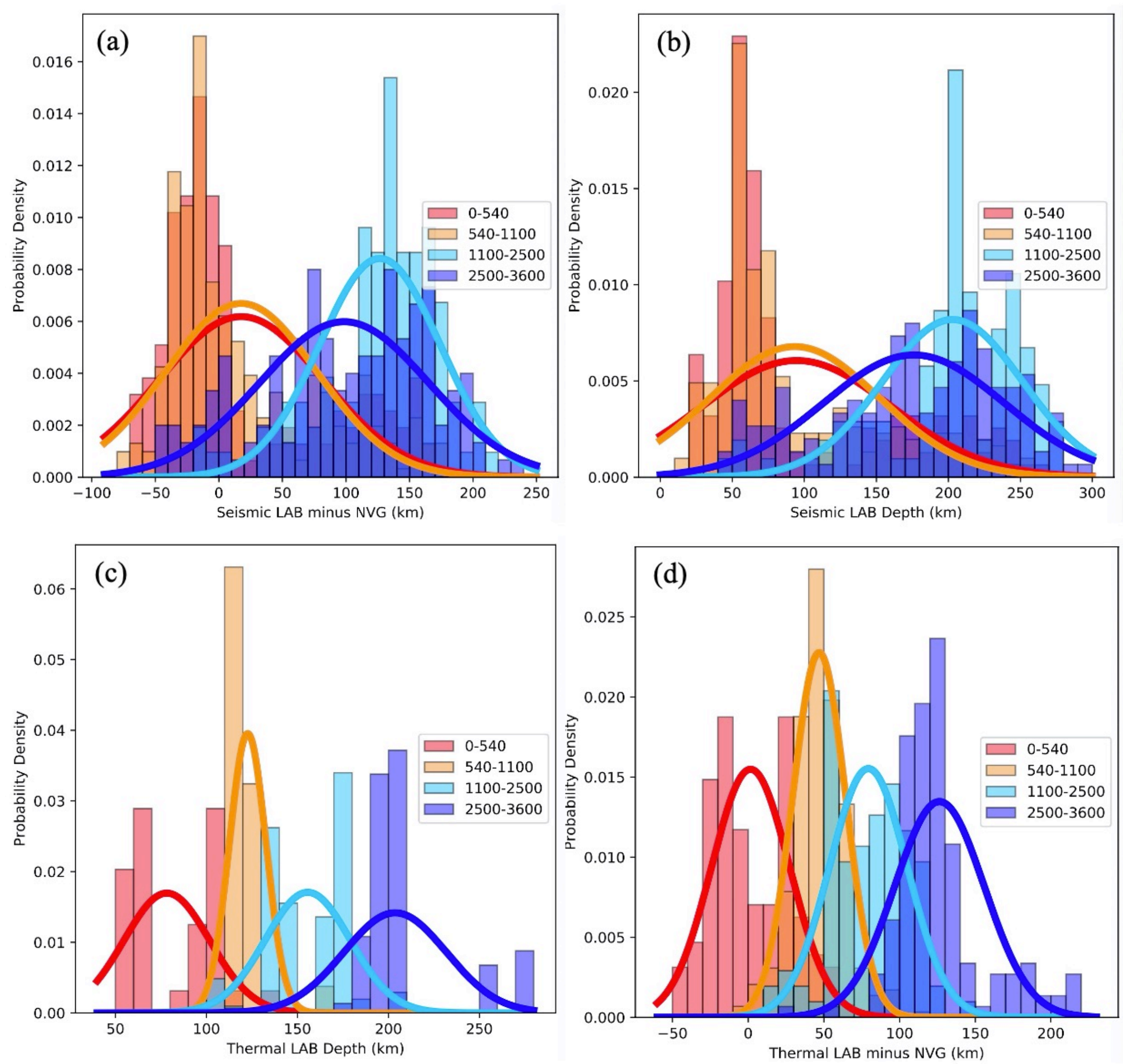

Figure 7. Different LAB models and comparison with NVG for Nubia/Somalia/Arabia. Histograms of (a) tomographic LAB depths (Pasyanos, 2010), (b) tomographic LAB minus NVG depths (blue means LAB deeper than NVG), (c) thermal LAB depths (Artemieva, 2006) and (d) thermal LAB minus NVG depths, all organized by thermal ages (0–540, 540–1100, 1100–2500 and 2500–3600 Ma).

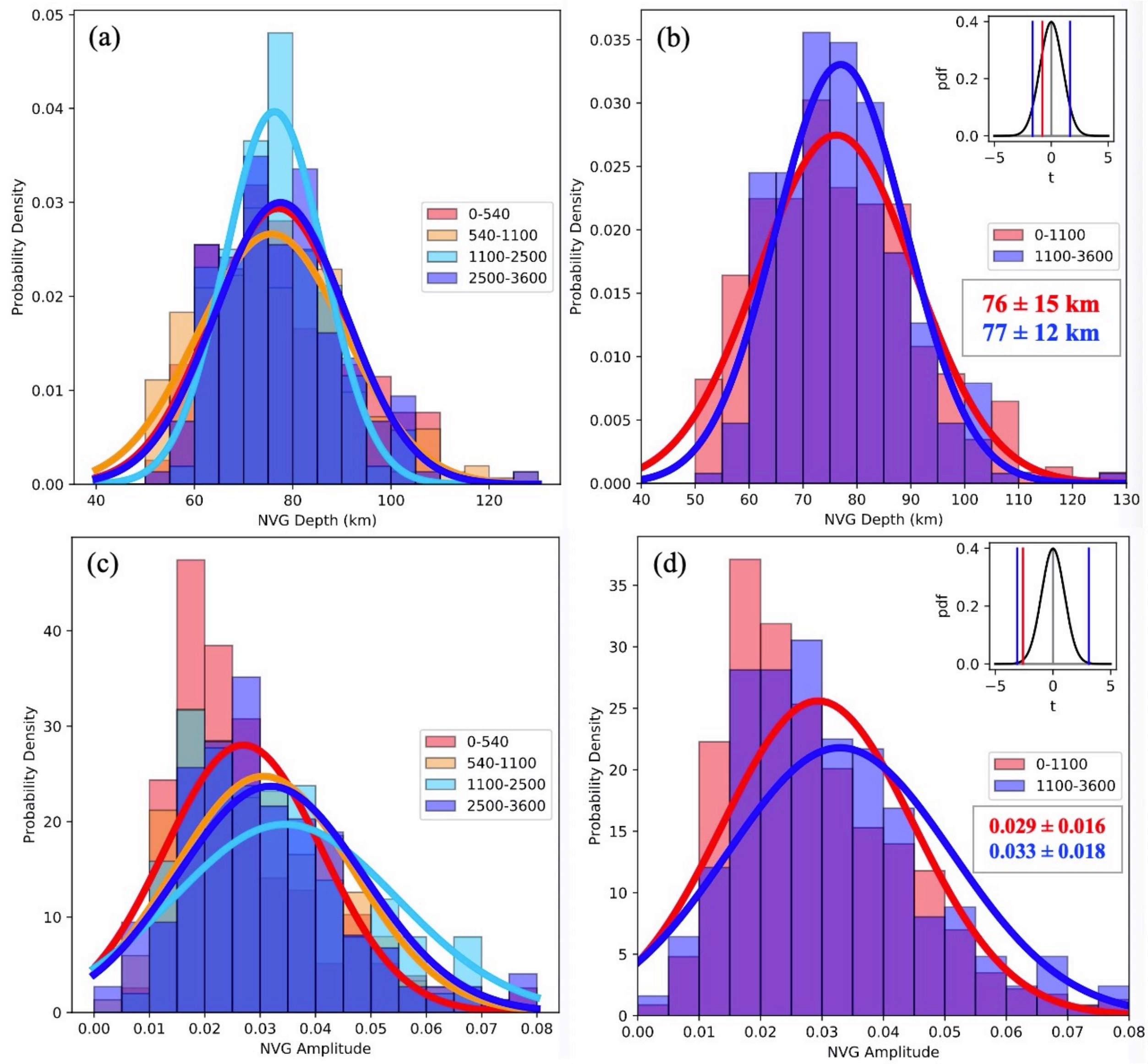

Figure 8. NVG statistics for Nubia/Somalia/Arabia. Histograms of (a and b) NVG depths and (c and d) relative stacking amplitudes corresponding to TC1 thermal age. Statistical comparison of young (0–1100 Ma) and ancient (1100–3600 Ma) binned regions for (b) NVG depths and (d) NVG amplitudes include t-tests (upper-right insets), showing the NVG depth populations are indistinguishable but the NVG amplitude populations are potentially distinct.

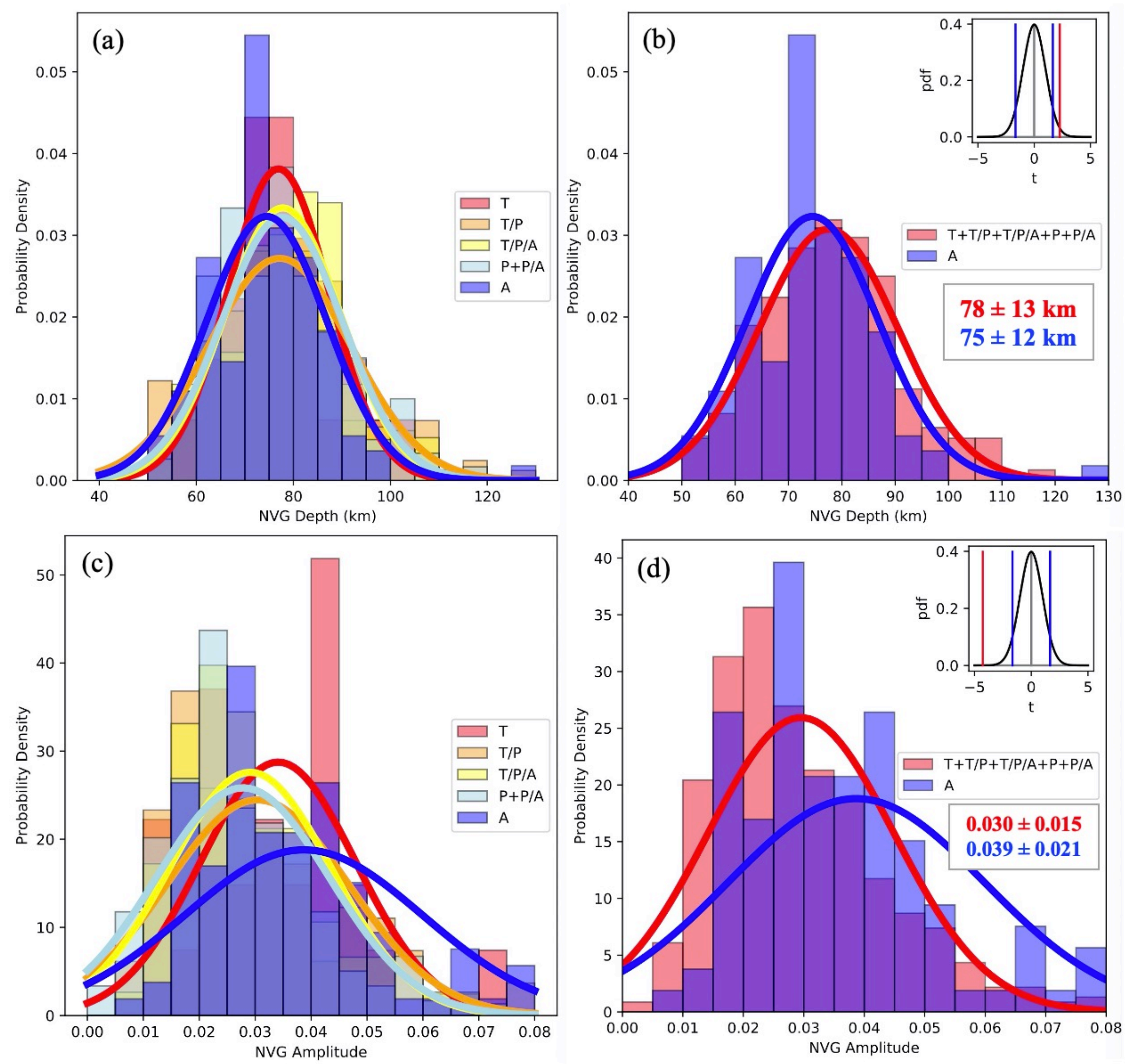

Figure 9. NVG statistics for Nubia/Somalia/Arabia. Histograms of (a and b) NVG depths and (c and d) relative stacking amplitudes corresponding to tectonothermal regionalization of Griffin et al. (2013). Statistical comparison between young or modified lithosphere and unmodified Archons (>2500 Ma) for (b) NVG depths and (d) NVG amplitudes include t-tests (upper-right insets), show both the depth and the amplitude populations are potentially distinct.

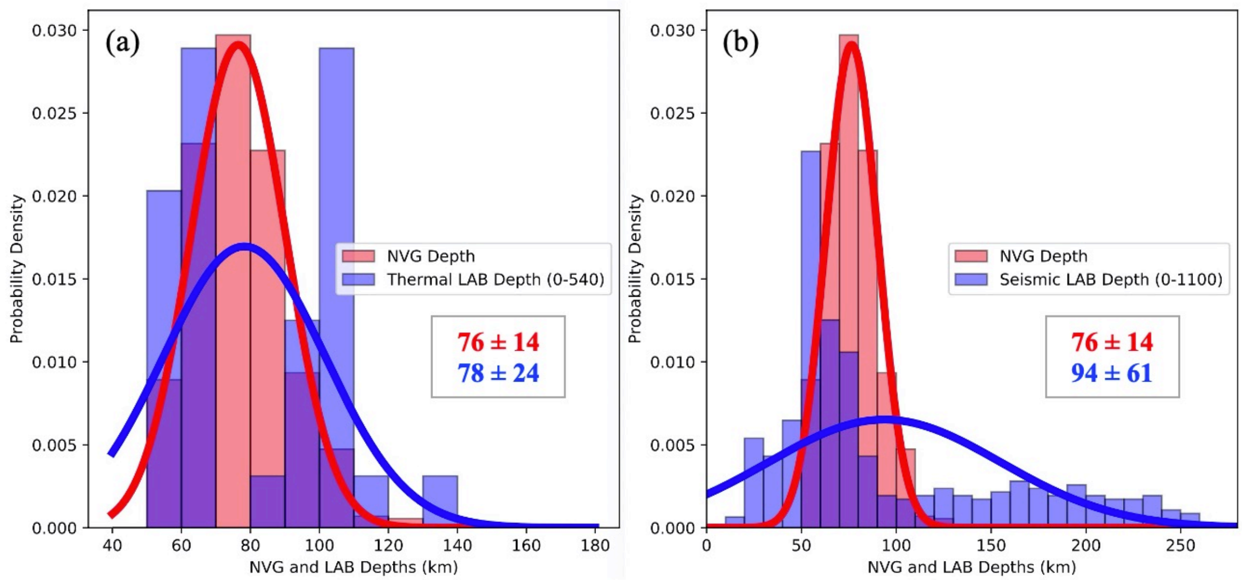

Figure 10. NVG compared to different LAB models by age for Nubia/Somalia/Arabia. Comparison of (a) Phanerozoic thermal LAB depths (Figure 7c) and (b) Phanerozoic and Neoproterozoic tomographic LAB depths (Figure 7a) with NVG depths of all ages. Because the LAB depths appear bimodal (clearly non-Gaussian), t-tests are not appropriate to analyze these data.